



Cite this: DOI: 10.1039/d4ee04205k

# An ultra-high output self-managed power system based on a multilayer magnetic suspension hybrid nanogenerator for harvesting water wave energy†

Ying Lou,<sup>‡,ab</sup> Mengfan Li,<sup>‡,ac</sup> Aifang Yu,<sup>\*,abc</sup> Zhong Lin Wang<sup>\*,acd</sup> and Junyi Zhai<sup>‡,abc</sup>

Triboelectric–electromagnetic hybrid nanogenerators (TE-HNGs) are promising for efficient energy harvesting, particularly from high-energy-density water waves. However, existing TE-HNGs often suffer from mechanical combinations and lack comprehensive energy optimization strategies, resulting in a suboptimal overall effect where  $1 + 1 \leq 2$ . Herein, a highly coupled energy self-managed power system (ESPS) is proposed based on our meticulously designed multilayer magnetic suspension hybrid nanogenerator (MS-HNG) with triboelectric and electromagnetic units. Due to voltage phase coherence between the generators, the magnetic suspension electromagnetic generator (MS-EMG) serves as the gate drive source for metal oxide semiconductor field-effect transistors, enabling the instantaneous release of energy from the magnetic suspension triboelectric nanogenerator (MS-TENG) and thereby maximizing energy output within each cycle. The ESPS achieves a peak power of 261.3 mW, a significant improvement over 75.5 mW from the MS-HNG alone, illustrating a synergistic effect where  $1 + 1 > 2$ . Additionally, the ESPS achieves a current of 45 mA (a 7500% increase) and a power density of  $631 \text{ W m}^{-3}$  (a 346% increase). In water wave environments, this system can power 32 bulbs of 3 W each and perform water quality monitoring. This work represents a new breakthrough in the structural and circuit coupling of TE-HNGs, marking a milestone towards commercialization.

Received 15th September 2024,  
Accepted 5th December 2024

DOI: 10.1039/d4ee04205k

rsc.li/ees

## Broader context

Water wave energy exhibits significant sustainability and environmental benefits. Compared to solar and wind energy, which are available only 20–30% of the time, wave energy can be harnessed about 90% of the time, positioning it as a critical player in the global energy transition. Researchers aim to develop a triboelectric–electromagnetic hybrid generator (TE-HNG) that operates efficiently across both low-frequency and high-frequency wave ranges. However, achieving simultaneous high efficiency from both generator units in a fixed frequency range is challenging, impeding the anticipated synergistic effect. Additionally, current energy management strategies to address impedance mismatch often require matching the generator output with specific electronic components, complicating the manufacturing of integrated chips. To address these issues, we designed an energy self-management power system (ESPS) based on a multilayer magnetic suspension hybrid nanogenerator (MS-HNG). This system achieves a peak power of 261.3 mW, surpassing the 75.5 mW peak output power of the MS-HNG, demonstrating the exceptional synergistic effects of the ESPS. Moreover, the innovative switch design and precise structural design enable it to deliver an ultra-high current of 45 mA and an extraordinary peak power density of  $631 \text{ W m}^{-3}$ . Under simulated wave conditions, the ESPS continues to operate efficiently, capable of illuminating 32 bulbs of 3 W and conducting water quality detection. This advancement offers a promising solution to the technical challenges associated with TE-HNGs and their integrated chip manufacturing.

<sup>a</sup> Beijing Key Laboratory of Micro-Nano Energy and Sensor, Center for High-Entropy Energy and Systems, Beijing Institute of Nanoenergy and Nanosystems, Chinese Academy of Sciences, Beijing 101400, P. R. China. E-mail: yuaifang@binn.cas.cn, jyzhai@binn.cas.cn

<sup>b</sup> Center on Nanoenergy Research, Institute of Science and Technology for Carbon Peak & Neutrality, Key Laboratory of Blue Energy and Systems Integration (Guangxi University), Education Department of Guangxi Zhuang Autonomous Region, School of Physical Science & Technology, Guangxi University, Nanning 530004, China

<sup>c</sup> School of Nanoscience and Engineering, University of Chinese Academy of Science, Beijing 100049, China

<sup>d</sup> Georgia Institute of Technology, Atlanta, GA30332, USA. E-mail: zhwang@gatech.edu

† Electronic supplementary information (ESI) available: Fig. S1–S18, Tables S1 and S2, and supplementary videos. See DOI: <https://doi.org/10.1039/d4ee04205k>

‡ These authors contributed equally to this work.

# 1 Introduction

Monitoring and studying the oceans are essential for our understanding of the Earth.<sup>1</sup> Ocean wave energy, with its high energy density, represents a promising renewable energy source.<sup>2,3</sup> However, conventional marine equipment faces limitations due to its dependence on external power sources and mobility restrictions.<sup>4</sup> To address these challenges, triboelectric nanogenerators (TENGs) have been proposed as sustainable power solutions for marine monitoring devices.<sup>5</sup> Despite their potential, TENGs generally produce relatively low output current and power,<sup>6,7</sup> which may be inadequate for high-power equipment. Additionally, their high impedance characteristics can lead to compatibility issues with terminal equipment.<sup>8</sup>

Mechanical design<sup>9,10</sup> and power management<sup>11,12</sup> are considered to be the crucial approaches for improving the energy harvesting and conversion efficiency of TENGs in the field of blue energy. Firstly, in terms of mechanical design, methods such as the use of multilayer designs,<sup>13,14</sup> mechanical regulation,<sup>15,16</sup> and triboelectric–electromagnetic hybrid nanogenerators (TE-HNGs)<sup>17,18</sup> have been proposed. However, current multilayer designs often rely on springs<sup>19</sup> or elastic supports like Kapton<sup>20</sup> or TPU.<sup>21</sup> The inherent length of the springs and the lifespan of the supporting materials limit the effectiveness of multilayer designs. Cylindrical structural TENGs<sup>22,23</sup> are typical examples of mechanical regulation but still need significant improvements in spatial efficiency. Additionally, TE-HNGs use dual energy conversion mechanisms to widen the operational frequency range, thereby maximizing energy collection.<sup>24,25</sup> Compared to electromagnetic generators (EMGs), TENGs are more suited for harvesting low-frequency energy.<sup>26–28</sup> Therefore, challenges arise when coordinating the two units for harvesting low-frequency water wave energy, impacting the optimal output of EMGs<sup>22</sup> and resulting in a combined effect where  $1 + 1 \leq 2$ . Thus, the desired synergistic effect between the units remains unrealized.

Moreover, existing energy management for TE-HNGs is predominantly biased towards TENGs while neglecting the EMGs.<sup>18,29</sup> The use of a “switch” is crucial for managing TENG energy, but an active switch requires external power, which contradicts the self-powered goal of the system.<sup>30</sup> Although a passive switch does not require external power, electronic components like silicon-controlled rectifiers (SCRs) and gas discharge tubes (GDTs) are limited by manufacturing processes and cost, resulting in low withstand voltage values and larger spacing issues. In circuit design, the specification of a “switch” is often selected based on the optimal output of the TENG, which does not allow for continuous adjustment of the switch’s conduction voltage to match different TENG outputs. This limitation hinders the design of integrated power management chips for later industrial applications. Overall, an optimal solution for TE-HNGs has not yet been reported to address these technical issues.

Herein, we propose an energy self-managed power system (ESPS) based on a multilayer magnetic suspension hybrid nanogenerator (MS-HNG). This hybrid nanogenerator

combines a multilayer magnetic suspension triboelectric nanogenerator (MS-TENG) and an electromagnetic generator (MS-EMG) by leveraging the repulsion principle between like poles of magnets. A smart connection between the MS-TENG and MS-EMG is established *via* a metal-oxide-semiconductor field-effect transistor (MOSFET) switch, allowing for the instantaneous release of energy from the former through the activation of the switch by the latter’s energy, thereby maximizing energy. Experimental results demonstrate phase coherence between the MS-TENG and the MS-EMG. Due to the presence of a self-activating switch, the impedance of ESPS reduced to 1 k $\Omega$ , significantly addressing the impedance mismatch between the traditional TENG and electrical loads. The system delivers a current of up to 45 mA, achieving a peak power density of 631 W m<sup>-3</sup>. This approach achieves a synergistic effect of  $1 + 1 > 2$ . Furthermore, the ESPS remains effective in simulated water wave environments, capable of illuminating 32 light bulbs with 3 W. After charging a 10 mF commercial capacitor, the water quality sensor can be triggered every 8 min. This work offers a novel pathway for optimizing TE-HNGs, even other dual-mode TENGs, and provides essential support for the development of integrated power management chips.

## 2 Results and discussion

### 2.1 Structure design and working principle of the ESPS

As of this year, TENG technology has been used for wave energy harvesting for a full decade. As illustrated in Fig. 1a, incorporating a multilayer design, hybrid structure, and implementing effective power management are key strategies to improve the electrical output efficiency of wave energy harvesters. However, the issues related to these techniques have been discussed in the introduction section. Therefore, it is crucial to refine the device design and optimize the system management strategy to address these technical challenges effectively.

To address this issue, we improved upon our previous work<sup>15</sup> by combining an MS-TENG with an MS-EMG to create an MS-HNG, utilizing the principle of magnetic repulsion between like poles. The schematic diagram and photograph are shown in Fig. 1b and Fig. S1 (ESI<sup>†</sup>), respectively. The MS-HNG skeleton is constructed using multi-layer acrylic substrates with four corner constraints. Due to magnetic repulsion, gaps between the substrate layers prevent them from adhering to each other. Notably, as the number of layers increases, the gravity borne by the lower-layer units gradually becomes larger. To address this, we precisely control the number of magnets embedded in each layer using the magnetic suspension skeleton shown in Fig. S2 (ESI<sup>†</sup>), thereby regulating the magnetic field strength to maintain a layer spacing of approximately 3 mm. Before securing the substrates, friction layers are installed on each layer. Conductive foam pads, used instead of conventional copper electrodes and sponges, are attached to opposite sides of adjacent substrates to enhance flexibility. A nylon film and fluorinated ethylene propylene (FEP) film serve as positive and negative friction layers for the TENG,

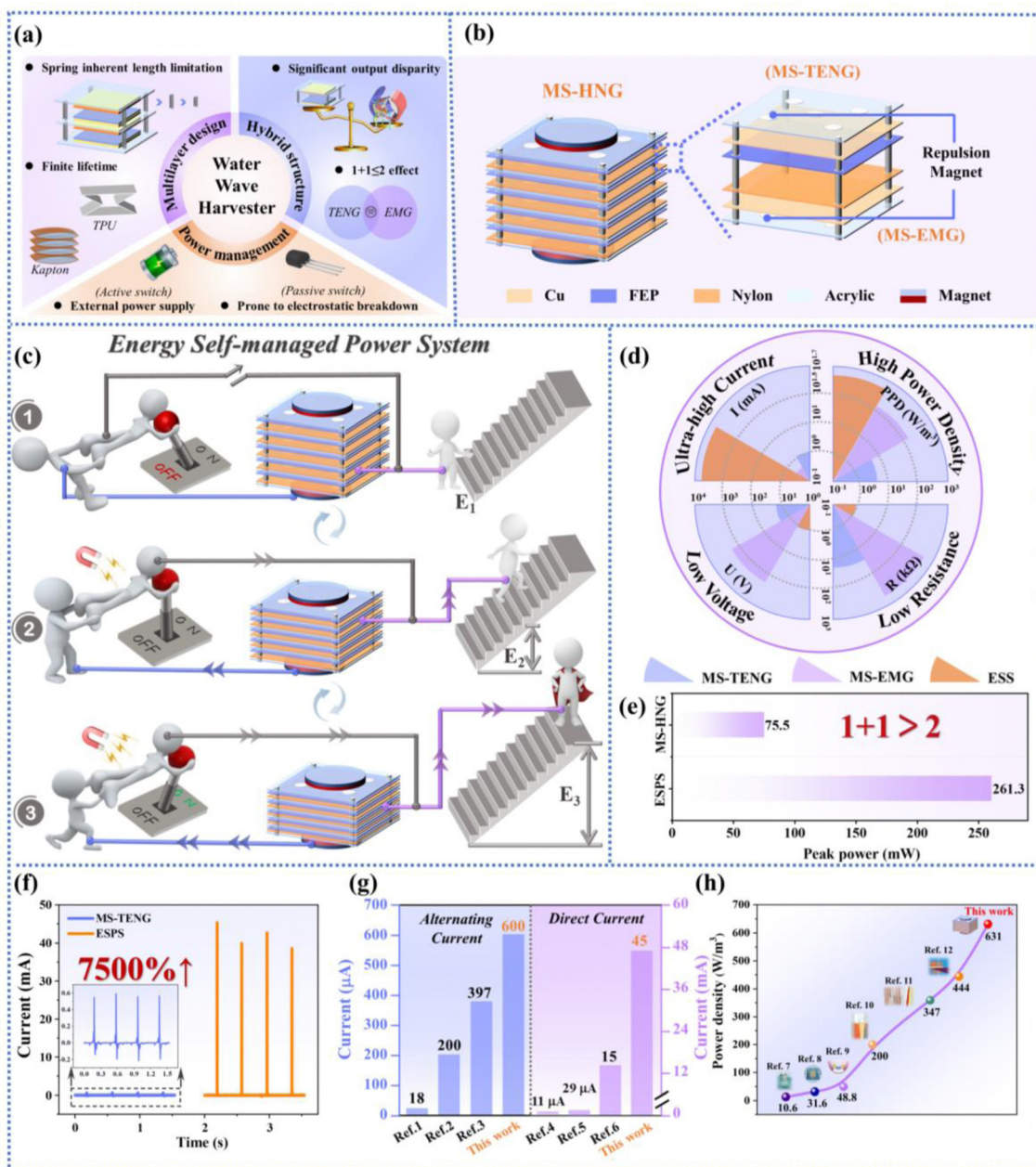


**Fig. 1** The ESPS based on the MS-HNG. (a) TENG technical barriers to common methods of water wave energy harvesting. (b) The whole structural diagram of an MS-HNG. (c) The working mechanism of the ESPS. (d) Output characteristics of the ESPS. (e) Comparison of the output powers of the MS-HNG and ESPS. (f) Comparison of the output currents of the MS-TENG and ESPS. (g) Comparison of the output currents of the MS-TENG and ESPS with those in other studies, respectively. (h) Comparison of the peak power densities between the ESPS and other excellent multilayer TENGs.

respectively, and are adhered to the conductive foam pads to form an MS-TENG. The working principle of the MS-TENG is illustrated in Fig. S3 (ESI<sup>†</sup>). Due to the multi-layer magnetic repulsion, minor disturbances may not create sufficient contact between the friction layers of the MS-TENG. To address this, two magnets with specific gravity and opposing magnetic pole orientations are installed above and below the MS-TENG, along with corresponding coils, to form the MS-EMG, supported by a counterweight. The working principle of the MS-EMG is shown in Fig. S4 (ESI<sup>†</sup>). The introduction of large magnets not only

facilitates better contact between the friction layers of the MS-TENG, but also, benefiting from the design of the multi-layer magnetic suspension system, achieves a phenomenon of multiple-output under a single-trigger during the dynamic balance process between gravity and repulsion.

To further enhance its electrical output, we developed an energy self-managed power system (ESPS) based on an MS-HNG. At its essence, this system harnesses the energy derived from the MS-EMG to trigger the MOSFET, thereby enabling the instantaneous release of energy from the MS-TENG to

maximize energy output. As illustrated in Fig. 1c, when external disturbances occur, the layers within the MS-HNG transition from complete separation to full contact due to the gravitational force, followed by rapid separation driven by magnetic repulsion. The three characters illustrated—on the left, middle, and right—represent the MS-EMG, the switching circuit, and the MS-TENG, respectively. In the state of complete separation, the electrical output of the MS-EMG is minimal, the switch is off, and the energy of the MS-TENG is at its nadir. Upon external disturbance, the gaps between the units gradually diminish until full contact ensues. At this critical juncture, the output voltage of the MS-EMG reaches the threshold required to trigger the MOSFET, prompting the switch to rapidly open, causing the energy of the MS-TENG to reach its maximum instantaneously. Compared to individual MS-TENG and MS-EMG setups, the ESPS offers significant advantages, including lower voltage, lower impedance, ultra-high current, and higher power density (Fig. 1d). In the absence of energy management, the peak power outputs are 72.6 mW for the MS-TENG and 2.9 mW for the MS-EMG, totaling 75.5 mW for the MS-HNG. In contrast, the ESPS achieves a peak power output of up to 261.3 mW, representing a 346% increase and demonstrating a synergistic effect where  $1 + 1 > 2$  (Fig. 1e).

The MS-TENG is the energy source for the ESPS, while the MS-EMG is the means to achieve high output for the ESPS. Under the action of the self-activating switch, the current of the MS-TENG transitions from its initial 0.6 mA alternating current to a remarkable 45 mA direct current, representing a 7500% increase and highlighting the pivotal role of the ESPS (Fig. 1f). To validate the device design and ESPS performance, we compared it with other leading studies in wave energy harvesting.<sup>31–33</sup> Even without energy management, the MS-TENG generates an alternating current of 0.6 mA, thanks to its structural design utilizing the magnetic suspension effect within the multilayer power generation units. Furthermore, the direct current output of ESPS remarkably outshines the existing literature,<sup>34–36</sup> achieving an unprecedented 45 mA, marking a notable advancement in the field (Fig. 1g). Additionally, compared to other multilayer wave energy harvesters,<sup>21,25,37–40</sup> the ESPS achieves a peak power density of  $631 \text{ W m}^{-3}$  (Fig. 1h). This ground-breaking research clearly underlines the promising trajectory of ESS applications in the field of wave energy harvesting.

## 2.2 Electrical properties of the MS-TENG and MS-EMG

To optimize the electrical output of the MS-HNG and investigate the impact of the triggering environment, a vertical stepper motor was employed to drive the MS-HNG for systematic analysis. By leveraging the principle of repulsion between like magnetic poles, constructing an MS-TENG to enhance space utilization is relatively straightforward. As demonstrated in Fig. S5 (ESI<sup>†</sup>), increasing the number of TENG units resulted in higher short-circuit current ( $I_{sc}$ ), and transferred charge ( $Q_{sc}$ ), escalating from 0.16 mA and 0.70  $\mu\text{C}$  to 0.63 mA and 3.55  $\mu\text{C}$ , respectively. Thus, ingeniously deploying magnets is advantageous for optimizing space utilization. Given the

eventual deployment of this device for harnessing wave energy in the unpredictable ocean environment, enhancing its susceptibility to external disturbances is crucial. To achieve this, repelling magnets and corresponding coils were added to the upper and lower sides of the MS-TENG, forming an MS-EMG. Larger magnets generate greater repulsive force, necessitating suitable counterweights on the upper side to ensure full contact and effective separation of the MS-TENG is imperative. Notably, when the counterweight mass increased from 40 g to 160 g (shown in Fig. S6, ESI<sup>†</sup>), the  $I_{sc}$  and  $Q_{sc}$  elevate from 0.23 mA and 2.51  $\mu\text{C}$  to 0.63 mA and 3.55  $\mu\text{C}$ , respectively. Therefore, a 160 g counterweight was chosen for subsequent experiments. It is important to note that excessively large weights impede the separation of the MS-TENG, making further discussion on this issue unnecessary.

The MS-EMG comprises two relatively large magnet blocks with mutually repulsive properties, aided by a counterweight. Once disturbed by external forces, the multilayer units within the MS-TENG readily achieve close contact due to gravity. This interaction induces a change in magnetic flux within the MS-EMG, leading to the generation of induced electromotive force, subsequently converted into electrical energy output. Immediately after that, the repulsion force from the large magnets prompts a rapid rebound of the MS-TENG, facilitating significant separation of its layers *via* embedded small magnets within the substrate, enabling another cycle of EMG output (Fig. 2a). Fig. 2b shows the multiple oscillations of the MS-EMG when it is triggered once by the motor and then stops, due to the dynamic balance between gravity and repulsion. Fig. 2c, on the other hand, demonstrates the stable frequency multiplication effect of both the MS-TENG and MS-EMG when the motor is continuously triggered at a fixed frequency of 2.6 Hz.

The influence of different trigger frequencies on the electrical output of the MS-TENG and MS-EMG was investigated. Fig. 2d shows that as impedance increases, the voltage output of the MS-EMG initially rises rapidly, peaking at  $10^4 \text{ k}\Omega$  without further increase. At frequencies of 2.6 Hz, 2.1 Hz, and 1.6 Hz, voltages of 25.6 V, 10.6 V, and 4.7 V, respectively, were recorded. Correspondingly, at a matching impedance of 40 k $\Omega$ , the peak power densities were measured to be  $7.0 \text{ W m}^{-3}$ ,  $1.1 \text{ W m}^{-3}$ , and  $0.3 \text{ W m}^{-3}$ , respectively (Fig. 2e). Concurrently, Fig. 2f demonstrates that the current output of the MS-TENG varies with frequencies, reaching 0.63 mA, 0.44 mA, and 0.14 mA at 2.6 Hz, 2.1 Hz, and 1.6 Hz, respectively. Moreover, with increasing impedance, the current initially decreases rapidly and then levels off. Notably, Fig. 2g showcases peak power densities at matching impedances of 700 k $\Omega$ , 1 M $\Omega$ , and 4 M $\Omega$ , reaching  $175.2 \text{ W m}^{-3}$ ,  $122.2 \text{ W m}^{-3}$ , and  $38.3 \text{ W m}^{-3}$ , respectively. Therefore, higher frequencies are inferred to be more advantageous for the power output of both the MS-TENG and MS-EMG. The durability of the MS-HNG is a crucial characteristic for ensuring long-term effective energy harvesting. Fig. S7 (ESI<sup>†</sup>) displays the current of the MS-TENG and MS-EMG at various cycles. It is evident that the current remains nearly constant even after 150 000 cycles, confirming the outstanding durability of the MS-HNG.

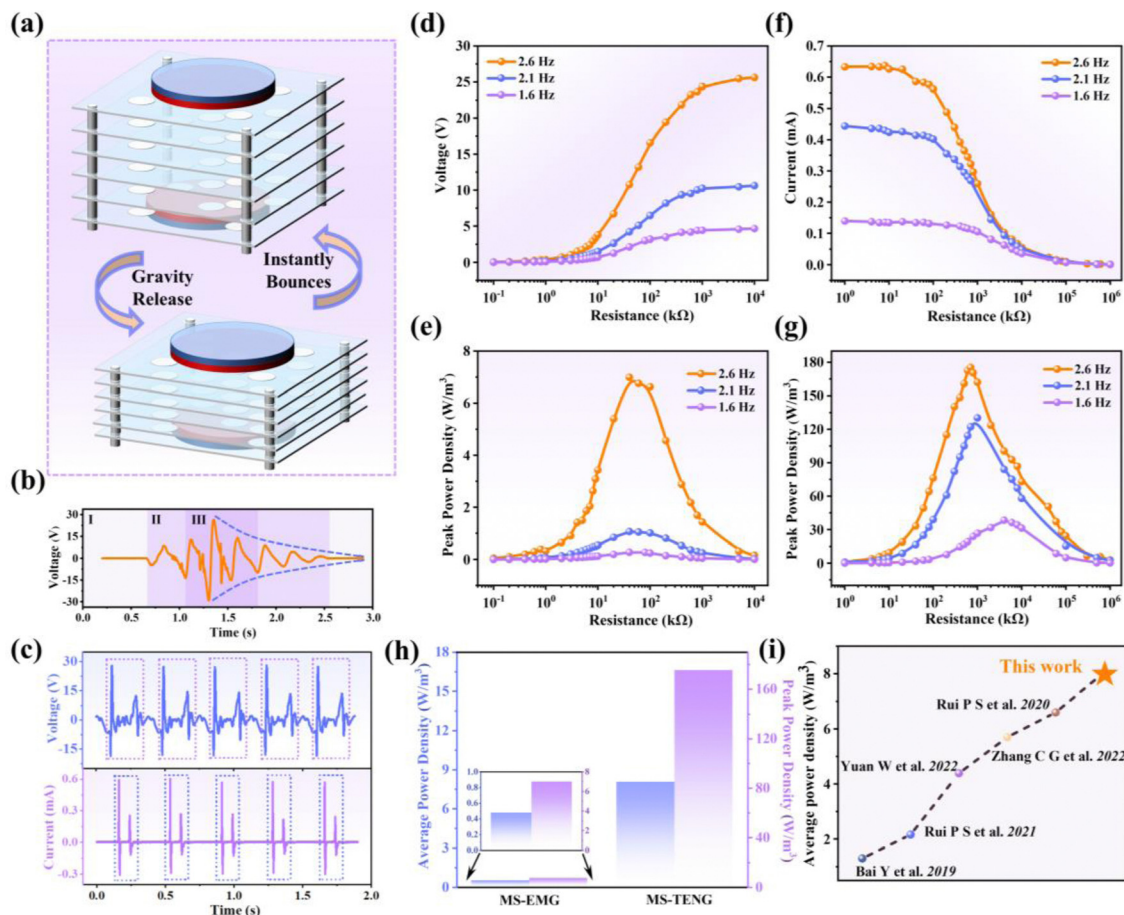


Fig. 2 The electrical properties of the MS-TENG and MS-EMG. (a) The operation of the MS-HNG. (b) The frequency multiplier effect of the MS-EMG. (c) The voltage and current of the MS-EMG and MS-TENG at 2.6 Hz, respectively. The voltage (d) and peak power density (e) of the MS-EMG at different frequencies. The current (f) and peak power density (g) of the MS-TENG at different frequencies. (h) Comparison of the power density between the MS-EMG and MS-TENG. (i) Comparison of the peak power density between the MS-TENG and other excellent TENGs.

As demonstrated in Fig. 2h and Fig. S8 (ESI<sup>†</sup>), the average power density of MS-TENG and MS-EMG reaches  $8.0 \text{ W m}^{-3}$  and  $0.5 \text{ W m}^{-3}$  at 2.6 Hz, respectively. In this setup, the contribution of the MS-EMG to the output of the MS-HNG is approximately 5%, while that of the MS-TENG is approximately 95%. Furthermore, compared to other excellent literature reports, the MS-TENG exhibits lower matching impedance (Fig. S9, ESI<sup>†</sup>) and a better average power density (Fig. 2i). Consequently, the MS-TENG shows relatively good electrical performance, but there is a significant disparity between the MS-EMG and MS-TENG, as with other TE-HNGs (Table S1, ESI<sup>†</sup>). Hence, it is imperative to leverage the signal from MS-EMG to enhance the output of MS-TENG.

### 2.3 Construction of the ESPS

The passive energy management circuit, based on the buck switch architecture, emerges as a paradigmatic solution for enhancing the energy conversion efficiency of TENGs across diverse applications. However, fabricating this circuit requires electronic components that operate based on specific threshold voltages, which rely on the voltage output of the TENG. Due to

their discontinuous operation and lack of adjustability, these components hinder the design of universal and integrated chips for TENGs with high voltage characteristics. To develop a more versatile energy management circuit and accelerate the commercialization of TENGs, we conceived a pioneering ESPS, leveraging the distinctive output attributes of the MS-HNG. This integrated system incorporates the MS-TENG and MS-EMG alongside a switch circuit centered on a MOSFET. Within the system, the MS-TENG handles energy harvesting tasks, while the MS-EMG manages crucial switch control functions.

As shown in Fig. 3a and Fig. S10 (ESI<sup>†</sup>), the MS-TENG is rectified through a bridge rectifier (RB) and connected in parallel with a storage capacitor  $C_{in}$ . The positive terminal of  $C_{in}$  is linked to the drain of the MOSFET, forming an energy harvesting unit. In the switch control section, the MS-EMG is connected in series with two diodes ( $D_2$ ,  $D_3$ ) to form a half-bridge rectifier circuit. This is followed by parallel connection with a voltage divider resistor  $R_D$  and a filtering capacitor  $C_F$ .  $R_D$ , in series with the coil resistance of the MS-EMG, acts as a voltage divider for the output voltage of the MS-EMG to control the voltage applied to the gate of the MOSFET.  $C_F$  filters out

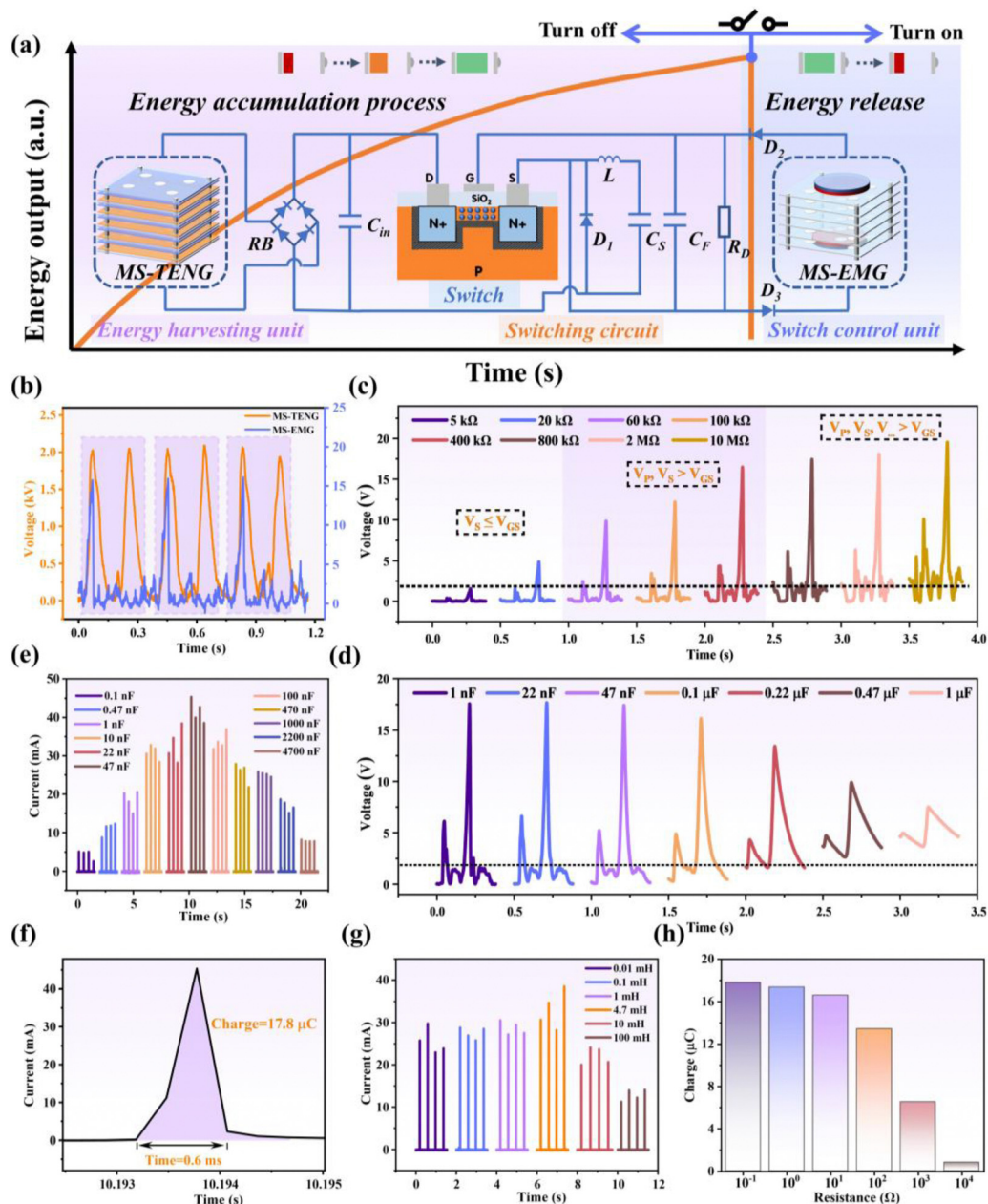


Fig. 3 The construction of the ESPS. (a) Working principle of the ESPS. (b) The phase consistency the MS-TENG and MS-EMG. Effect of the (c) voltage divider resistor ( $R_D$ ) and (d) filter capacitor ( $C_F$ ) on the voltage applied to the MOSFET at 2.6 Hz. (e) Output current at different capacitances of  $C_{in}$ . (f) Enlarged plot of the current of ESPS with a 47 nF capacitor. Electrical outputs of the ESPS at different (g) inductance and (h) resistances.

non-triggering signals in the circuit, preventing inadvertent triggering of the MOSFET, with its positive terminal connected to the gate of the MOSFET. MOSFETs, as high-speed, low-loss, and durable voltage-controlled semiconductor devices, achieve circuit on-off control by applying voltage signals to the gate. For an enhanced N-MOSFET, the operation is based on controlling the current carriers in the N-channel *via* gate voltage to achieve on-off control of the current flow. When the applied voltage exceeds the threshold voltage of the MOSFET, a forward-biased P-N junction is formed, creating a conducting path between the drain and source. Unlike previous studies

where MOSFETs were utilized for circuit switching controlled by external power sources and logic circuits, in the case of the MS-HNG, when the voltage of the MS-EMG reaches its peak ( $V_{RD} > V_{GS}$ ), causing the MOSFET to enter a conducting state. This facilitates an instantaneous release of energy accumulated in the storage capacitor  $C_{in}$ , allowing current to flow from the drain to the source and subsequently into the rear step-down circuit (Fig. S11, ESI<sup>†</sup>).

Whether the ESPS can achieve maximized energy output is contingent upon the conduction of the MOSFET when the output voltage of the MS-EMG reaches its maximum. As

illustrated in Fig. 3b, the structural design of the MS-TENG and MS-EMG enables their electrical outputs to exhibit phase consistency, wherein the voltage peaks reach their maximum values simultaneously. This synchronization allows the voltage signal from the MS-EMG to serve as the control signal for the MOSFET, effectively creating a self-activating switch. The coordinated operation between the MS-TENG and MS-EMG enables the instantaneous release of the accumulated energy within  $C_{in}$ , thus achieving the goal of energy self-management for the MS-HNG. With a MOSFET turn-on voltage of 2 V, their successful activation depends on whether the voltage at both ends of  $R_D$  can reach their threshold voltage (Fig. S12, ESI<sup>†</sup>). The related parameters are discussed according to the circuit connection mode shown in Fig. S13 (ESI<sup>†</sup>). Fig. 3c demonstrates that as the resistance increases from 5 k $\Omega$  to 10 M $\Omega$ , the voltage gradually escalates while maintaining at least two outputs within a single cycle. For resistances below 20 k $\Omega$ , the main peak voltage can reach 2 V or above; for resistances ranging from 20 k $\Omega$  to 400 k $\Omega$ , both the peak and secondary voltages can achieve 2 V or higher. However, once the resistance exceeds 800 k $\Omega$ , even though some spurious peaks may still exceed the threshold voltage of the MOSFET. Therefore, the filter capacitor plays a crucial role in mitigating these spurious peaks. At a voltage divider resistance of 400 k $\Omega$ , Fig. 3d demonstrates that a higher capacitance value of the filter capacitor augments the filtering efficacy. To maintain the magnitude of electrical output and ensure effective filtering of spurious peaks, a capacitance of 47 nF was selected for the capacitor ( $C_F$ ) in subsequent experiments. Similarly, we have given corresponding references to the circuit parameters for other triggering environments in Fig. S14 and S15 (ESI<sup>†</sup>).

Further investigation was conducted to explore the parameters influencing the instantaneous release of the energy harvesting terminal. As shown in Fig. 3e, the current of the ESPS shows a trend of first rising and then falling when the capacitance of  $C_{in}$  is increased from 0.1 nF to 10  $\mu$ F. The output current of the ESPS reaches a peak of 45 mA at a capacitance value of 47 nF. In the absence of the self-activating switch, the MS-TENG only achieves 0.6 mA, marking a 7500% enhancement. Before the MOSFET switch is turned on, the input capacitor  $C_{in}$  stores the maximum energy. When the MOSFET is activated, the energy stored in  $C_{in}$  is released instantaneously. During this process, the sudden conduction of the MOSFET results in a significantly higher current value in the energy management circuit compared to the unmanaged state. Integrating the current over a single cycle yields the charge quantity, as illustrated in Fig. 3f and Fig. S16 (ESI<sup>†</sup>), where a transferred charge of 17.8  $\mu$ C is discharged within a brief duration of 0.6 ms, providing compelling evidence of the effectiveness of the ESPS. For this system, the inductor serves to decrease the output voltage and enhance the output current. As shown in Fig. 3g, with an increase in the inductance value, the ESPS current demonstrates a trend of initial increase followed by decrease, reaching peak output at 4.7 mH. Generally, larger inductance stores more energy, better maintaining the stability of the electrical output. However,

larger-specification inductors typically require more coil turns to achieve the desired inductance value, which adds resistance to the inductor itself, leading to a decline in electrical output. As depicted in Fig. 3h, with the increase of the external load resistance, the resistance of the charge flowing in the circuit increases, thus reducing the transferred charge of the MS-TENG within a single cycle.

Therefore, this system enables intelligent adjustment *via* a variable resistor during subsequent integration into the chip manufacturing process, thus offering enhanced flexibility. This method can be utilized for other hybrid generator with voltage phase coherence, not limited to the TE-HNGs. It can also be adapted to other dual-mode generators, such as triboelectric-piezoelectric hybrid generators and dual-operation mode hybrid TENGs.

## 2.4 Output performance of the ESPS

To assess the electrical performance of the ESPS, we conducted a comprehensive comparison of its electrical performance against that of the MS-EMG and MS-TENG. The schematic depicting the primary circuit connections is presented in Fig. 4a. As illustrated in Fig. 4b and c, while the intrinsic output voltages of the MS-TENG and MS-EMG stand at 2443 V and 25 V, respectively, the voltage output of the ESPS can be modulated down to 23 V, reflecting a remarkable reduction by a factor of 106. This reduction is achieved by controlling the ON/OFF time ratio of the MOSFET by the MS-EMG, enabling the adjustment of output voltage and achieving highly efficient energy conversion. Despite the MS-TENG and MS-EMG exhibiting intrinsic output currents of 0.6 mA and 0.9 mA, respectively, the ESPS delivers a current output of 45 mA, signifying a notable 7500% amplification. The MOSFET switch is "OFF", the input capacitor  $C_{in}$  stores the maximum energy. When the MOSFET switch is "OFF," the input capacitor  $C_{in}$  stores the maximum energy. Upon turning the MOSFET "ON," the energy stored in  $C_{in}$  is released instantaneously. This sudden conduction of the MOSFET results in a significantly higher current value in the energy management circuit compared to the unmanaged state.

As depicted in Fig. 4d, without a self-activating switch, the MS-TENG and MS-EMG exhibit respective peak powers of 72.6 mW and 2.9 mW at impedances of 700 k $\Omega$  and 40 k $\Omega$ . The total peak power of MS-HNG is 75.5 mW, with corresponding peak power densities of 175.2 W m<sup>-3</sup> and 7.0 W m<sup>-3</sup>. Fig. S17 (ESI<sup>†</sup>) shows the output current and peak power density as a function of resistance. As the load resistance increases from 1  $\Omega$  to 1000 k $\Omega$ , the power of ESPS reaches its maximum value of 261.3 mW at a matched resistance of 1 k $\Omega$ , with a peak power density of 631 W m<sup>-3</sup>, far exceeding the cumulative peak power densities of the MS-TENG and MS-EMG. This synergy illustrates a scenario where 1 + 1 > 2. The integration of a self-activating switch significantly enhances the peak power density while mitigating impedance mismatch, thus optimizing device adaptation for sensor applications.

To further investigate the efficacy of the ESPS, we employed the MS-TENG, MS-EMG, MS-HNG, and ESPS individually to

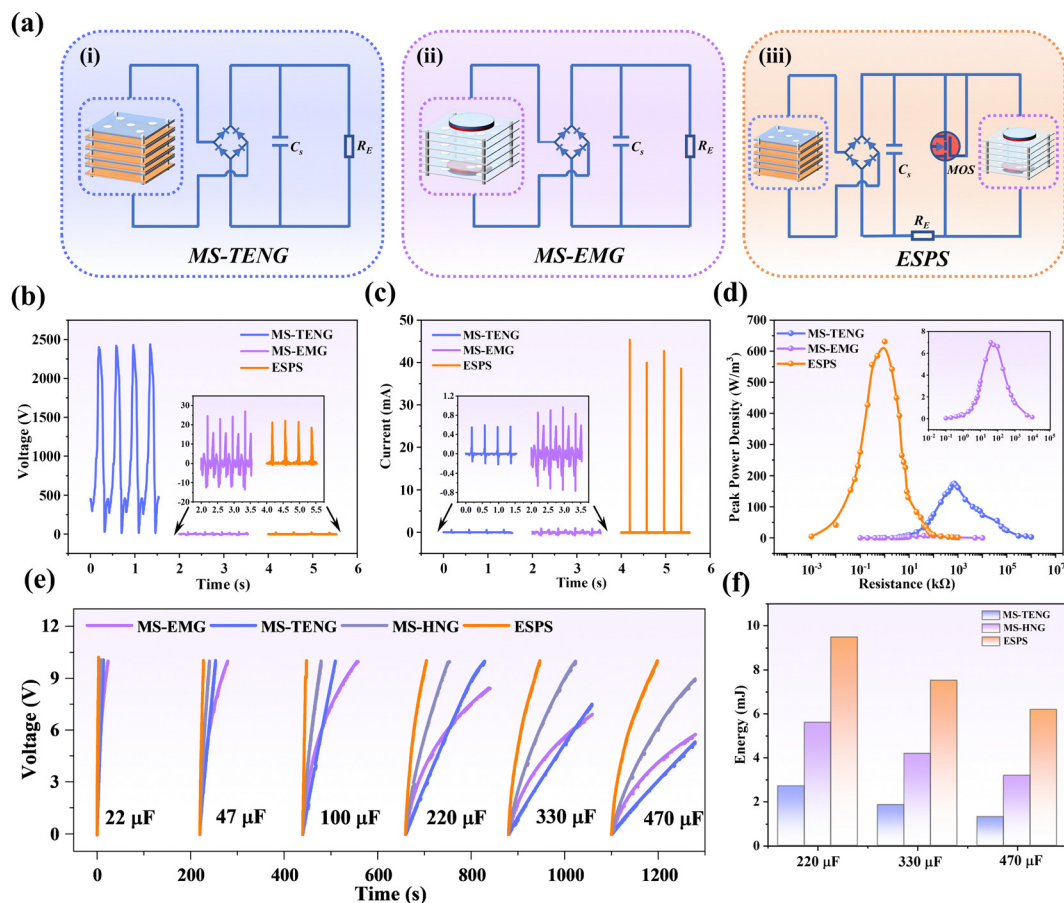


Fig. 4 Output performance of the ESPS. (a) The circuit diagrams for testing the MS-TENG, MS-EMG and ESPS. Comparison of (b) voltage, (c) current, and (d) peak power with and without a self-activating switch. (e) Charging curves of different power generation units for different capacitors. (f) A comparison of the energy storage abilities of the MS-TENG, MS-EMG and ESPS for different capacitors.

charge capacitors of varying specifications. As illustrated in Fig. 4e, for the same output unit, the charging rates decelerate with increasing capacitor specifications. Under fixed capacitor specifications, the ESPS exhibits the highest charging efficiency, followed by the MS-HNG, while the standalone MS-TENG or MS-EMG demonstrates the slowest charging rates, thus robustly validating the effectiveness of ESPS. In essence, the strategy of harnessing the internal unit MS-EMG of MS-HNG for managing the output energy of MS-TENG markedly surpasses direct energy provisioning from these two power generation units. As shown in Fig. 4f, with capacitor values of 220  $\mu$ F, 330  $\mu$ F, and 470  $\mu$ F, the ESPS consistently surpasses the MS-TENG and MS-HNG in energy storage effectiveness, further highlighting the superior value of the ESPS.

## 2.5 Applications of the ESPS

TENGs harness water wave energy to provide sustainable and stable power for sensors, holding significant implications for marine monitoring. Nevertheless, the parameter of water waves varies over time and environmental conditions, thus the feasibility of the ESPS operating smoothly in water still needs further investigation. The crux of this system lies in determining whether the MS-EMG can successfully trigger the MOSFET,

thereby enabling the instantaneous release of MS-TENG energy. To this end, an investigation of the MS-EMG within different water wave frequency (0.5 Hz–1 Hz) and wave height (5–10 cm) ranges was conducted, as shown in Fig. 5a. The results demonstrate that the voltages of in both cases exceeded the threshold voltage of 2 V without breaching the operational limit of 30 V, exhibiting an upward trend with an increase in frequency and wave height. Notably, even at the lowest frequencies and wave heights, the voltage of the EMG can reach the threshold voltage of the MOSFET, thus inferring the smooth operation of the ESPS in simulated water wave environments. Subsequently, the impact of different frequencies and wave heights on the electrical output of the ESPS was explored, as depicted in Fig. 5b and c. Within the defined range of water waves, the electrical output of the MS-TENG increased with the respective parameters. At a frequency of 1 Hz and a height of 10 cm, the ESPS achieved a current of 8 mA and a peak power density of 120 W m<sup>-3</sup>. As shown in Table S2 (ESI<sup>+</sup>), the ESPS demonstrates excellent electrical performance both in air and in water environments, compared to other multi-layer TENGs in the field.

Further elucidating the viability of the ESPS, Fig. 5d offers a comparative analysis between the MS-TENG and the ESPS.

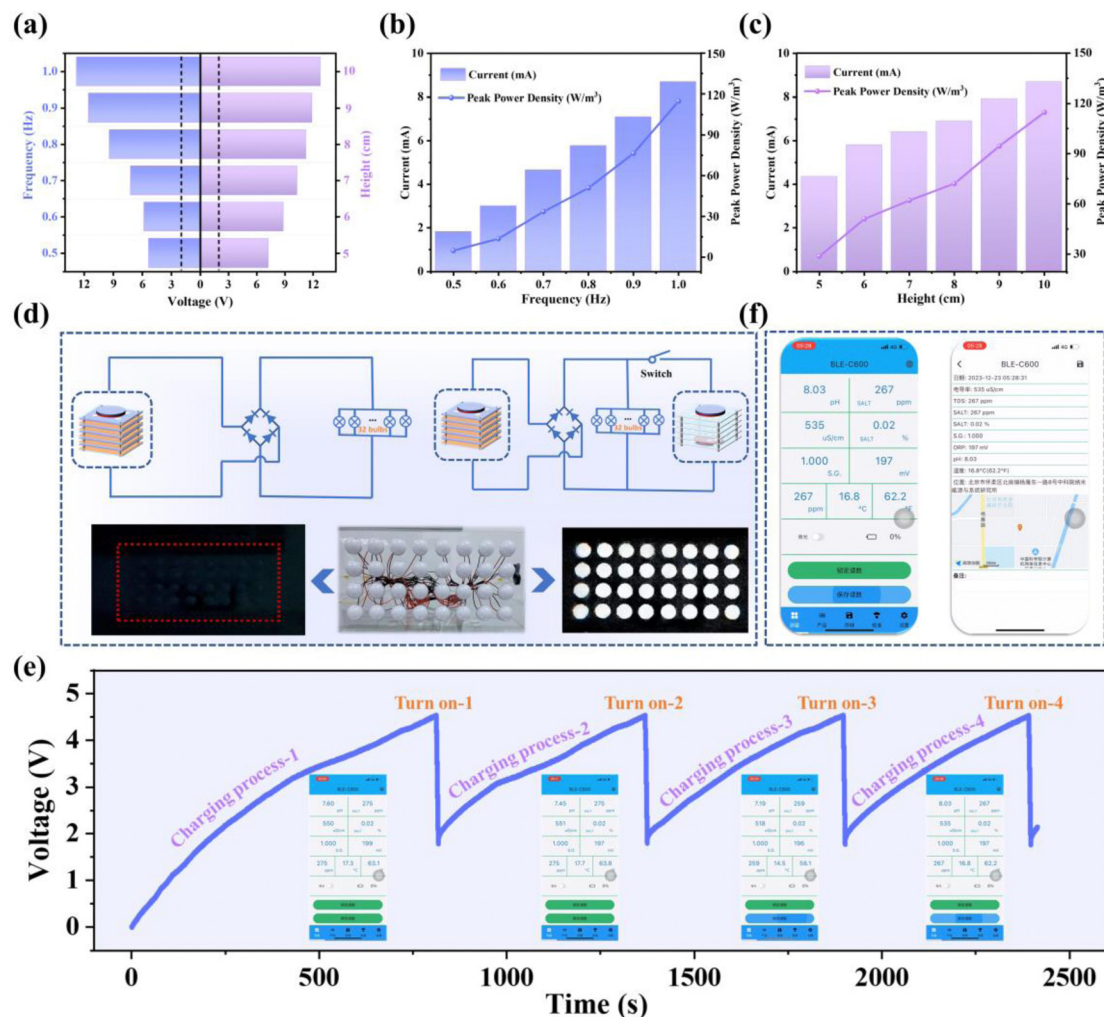


Fig. 5 Applications of the ESPS. (a) Comparison of the voltage of the MS-EMG in different water wave environments. Effect on the output performance of the ESPS at different (b) frequencies and (c) wave heights. (d) Comparison of light bulbs without and with a self-activating switch. (e) Charging curve and (f) mobile phone interface showing an ESPS powering a water quality sensor by charging a 10 mF capacitor.

Notably, the ESPS exhibits superior capability owing to its high current characteristics, enabling the illumination of 32 bulbs of 3 W (ESI,<sup>†</sup> Movie S1). Additionally, after charging a 10 mF capacitor, the water quality sensor can be triggered at 8-minute intervals, as displayed in Fig. 5e and f and ESI,<sup>†</sup> Movie S2. Once triggered, essential water quality information such as pH, conductivity, solid solubility, salinity, and temperature can be seamlessly transmitted to mobile terminals *via* Bluetooth. Moreover, the relevant location information can be observed. This energy self-management strategy provides vital guidance for the advancement of marine monitoring endeavors.

### 3 Conclusion

In summary, we designed an energy self-managed power system (ESPS) based on a multilayer magnetic suspension hybrid nanogenerator (MS-HNG) for harnessing water wave energy. The MS-HNG couples MS-TENG and MS-EMG based on the

principle of magnetic repulsion of like poles. Benefiting from the structural design of magnetic suspension, the MS-HNG achieves multiple outputs even under a single triggering event during the dynamic balance of gravity and repulsion. To enhance the electrical output of the MS-HNG, we apply the output voltage of the MS-EMG to the MOSFET to achieve instantaneous release of current for the MS-TENG, forming an energy self-management system. This system can yield an ultra-high current of 45 mA, alongside a peak power density of 631 W m<sup>-3</sup>. Furthermore, impedance is significantly mitigated to as low as 1 kΩ, thereby mitigating energy loss in powering the sensor, ultimately enhancing overall efficiency. The synergy between the MS-TENG and MS-EMG in the ESPS significantly exceeds the output of the MS-HNG alone, achieving a comprehensive effect of 1 + 1 > 2. In simulated wave environments, the peak power of the ESPS can still reach 120 W m<sup>-3</sup>, capable of lighting up 32 light bulbs of 3 W. After powering a commercial capacitor of 10 mF, the water quality sensor can be cyclically triggered every 8 minutes to obtain salinity,

temperature, and related location information. This work provides a forward-looking solution for the efficient collection of wave energy using TE-HNGs even other dual-mode TENGs.

## 4 Experimental section

### 4.1 Fabrication of the MS-HNG device

A 1 mm thick acrylic plate was laser-cut into a 90 mm square shape, featuring multiple evenly spaced 12 mm diameter holes and 4 smaller 4 mm diameter holes at each corner. Subsequently, multiple 1 mm thick cylindrical small magnets (12 mm in diameter) were uniformly embedded within the acrylic plate, all oriented in the same polarity. This process was replicated to produce multiple magnet-embedded acrylic substrates. The adjacent substrates were then vertically arranged based on the principle of magnetic repulsion. On both sides of each substrate, 1 mm thick conductive sponges were affixed, serving as electrodes while enhancing flexibility. Subsequently, a 15  $\mu\text{m}$ -thick nylon film was applied as a positive friction layer on the upper conductive sponge, while an 80  $\mu\text{m}$  thick FEP film served as the negative friction layer on the lower conductive sponge. Next, 5 mm thick acrylic plates were cut into 90 mm squares with a single 60 mm diameter hole at the center and four 4 mm diameter holes at each corner. Two 5 mm-thick large cylindrical magnets of 60 mm diameter were embedded in these plates in a repulsive configuration. Additionally, the remaining two acrylic substrates accommodated 5 mm thick coils (0.05 mm wire diameter, 35 800 turns). Finally, four stainless steel rods, each 5 cm in length, were threaded through the multi-layered substrates from top to bottom, sequentially passing through the coil, large magnet, small magnet, coil, and large magnet. Finally, the devices are tightly sealed using high-barrier acrylic plastic and hot-melt adhesive.

### 4.2 Construction of the energy self-management circuit

The rectifier bridge used for the MS-TENG is a DB107. The half-wave rectifier circuit consists of two 1N4007 diodes (1 kV). The voltage divider resistors are 1/4 W metal film resistors, and the inductor is a  $9 \times 12$  mm through-hole I-shaped inductor. The filtering capacitors and  $C_{\text{in}}$  use high-voltage ceramic capacitors and CBB capacitors with ratings of 101 (1 kV), 471 (1 kV), 102 (1 kV), 103 (1 kV), 223 (1 kV), 473 (1 kV), 104 (1 kV), 224 (400 V), 474 (400 V), 105 (400 V), 225 (450 V) and 475 (400 V). The electrolytic capacitors used are 22  $\mu\text{F}$  (25 V), 47  $\mu\text{F}$  (25 V), 100  $\mu\text{F}$  (25 V), 220  $\mu\text{F}$  (25 V), 330  $\mu\text{F}$  (25 V), and 470  $\mu\text{F}$  (16 V). The MOSFET model is FQD2N100TM. All these electronic components are soldered onto a  $20 \times 40$  mm<sup>2</sup> PCB board.

### 4.3 Setup of the experimental apparatus

The precise control of the vertically placed linear motor (GKT-37  $\times$  120) for vertical reciprocating motion, which drives the device, is achieved using a programmable logic controller (PLC). Fast and accurate data acquisition is realized using a multifunctional data acquisition module (NI USB-6212), and the data are visualized in real time using custom-written

LabView software. The wave-making apparatus consists of a semi-enclosed water tank made of 2 cm thick acrylic sheets, with dimensions approximately 2.3 m in length, 0.6 m in width, and 0.8 m in height. The apparatus also includes a DC power supply, a servo motor controller, a servo motor, a wave-making paddle, a threaded rod, and a fish-eye crank (Fig. S18, ESI<sup>†</sup>). The DC power supply converts 220 V AC to 12 V DC to power the servo motor.

### 4.3 Electric measurements of the ESPS

A vertically mounted stepper motor was used to drive the ESPS. The transferred charge of the MS-TENG, as well as the short-circuit current and open-circuit voltage of the MS-EMG, were measured using a programmable electrometer (Keithley 6514). The short-circuit current of the ESPS was measured using an IoT Power CC. The open-circuit voltage of the MS-TENG was measured with an oscilloscope (LeCroy 610Zi). A programmable digital controller was employed to simulate water waves in the wave pool.

## Author contributions

Y. L., M. L., A. Y., Z. L. W. and J. Z. conceived the idea and designed the experiments. Y. L. performed the device fabrication, and experiments, and analysed the data. M. L. helped with the experiments and data analysis. Y. L. and M. L. wrote the manuscript. A. Y. reviewed and corrected the manuscript. Z. L. W. and J. Z. supervised and guided this work. All authors discussed the results and commented on the manuscript.

## Data availability

The data that support the findings of this study are available in the ESI<sup>†</sup> of this article.

## Conflicts of interest

The authors declare no conflicts of interest.

## Acknowledgements

This work was supported by the National Key R & D Project from the Ministry of Science and Technology, China (2021YFA1201603), the National Natural Science Foundation of China (52073032 and 52192611) and the Fundamental Research Funds for the Central Universities.

## References

- 1 G. B. Xu, Y. J. Shi, X. Y. Sun and W. M. Shen, *Sensors*, 2019, **19**, 1711.
- 2 A. Afsharfard, N. Baziyar and K. C. Kim, *Int. J. Aeronaut. Space Sci.*, 2023, **24**, 1102–1110.
- 3 T. K. A. Brekken, H. T. Özkan-Haller and A. Simmons, *IEEE J. Ocean. Eng.*, 2012, **37**, 294–300.

- 4 Y. Lou, M. F. Li, J. X. Hu, Y. L. Zhao, W. Q. Cui, Y. L. Wang, A. F. Yu and J. Y. Zhai, *Nano Energy*, 2024, **121**, 109240.
- 5 Z. L. Wang, T. Jiang and L. Xu, *Nano Energy*, 2017, **39**, 9–23.
- 6 C. Xu, J. R. Yu, Z. W. Huo, Y. F. Wang, Q. J. Sun and Z. L. Wang, *Energy Environ. Sci.*, 2023, **16**, 983–1006.
- 7 J. F. Sun, L. J. Zhang, S. Q. Gong, J. Chen and H. Y. Guo, *Nano Energy*, 2024, **119**, 109010.
- 8 Q. W. Wang, D. Y. Hu, X. L. Huang, Z. T. Yuan, L. P. Zhong, Q. Q. Sun, F. Wang, S. X. Xu and S. Chen, *Adv. Funct. Mater.*, 2024, **34**, 2409088.
- 9 C. Cao, Z. J. Li, F. Shen, Q. Zhang, Y. Gong, H. Y. Guo, Y. Peng and Z. L. Wang, *Energy Environ. Sci.*, 2024, **17**, 885–924.
- 10 J. Chen, K. J. Wu, S. K. Gong, J. C. Wang, K. Wang and H. Y. Guo, *Research*, 2023, **6**, 0168.
- 11 T. S. Hu, H. F. Wang, W. Harmon, D. Bamgboje and Z. L. Wang, *IEEE Trans. Power Electron.*, 2022, **37**, 9850–9864.
- 12 X. L. Cheng, W. Tang, Y. Song, H. T. Chen, H. X. Zhang and Z. L. Wang, *Nano Energy*, 2019, **61**, 517–532.
- 13 X. Y. Wang, C. Y. Ye, P. F. Chen, H. Pang, C. H. Wei, Y. X. Duan, T. Jiang and Z. L. Wang, *Adv. Funct. Mater.*, 2024, **34**, 2311196.
- 14 H. X. Hong, T. L. Chen, J. J. Yang, Y. W. Hu, J. T. Hu, D. S. Li, F. R. Liu, L. Q. Liu and H. Wu, *Cell Rep. Phys. Sci.*, 2024, **5**, 101933.
- 15 M. Li, Y. Lou, J. Hu, W. Cui, L. Chen, A. Yu and J. Zhai, *Small*, 2024, **20**, 2402009.
- 16 Y. S. Sun, Y. Yu, Q. Gao, X. S. Zhang, J. C. Zhang, Y. Q. Wang, S. Y. He, H. Y. Li, Z. L. Wang and T. H. Cheng, *Nano Energy*, 2024, **121**, 109194.
- 17 T. Y. Li, X. Wang, K. K. Wang, Y. X. Liu, C. X. Li, F. H. Zhao, Y. M. Yao and T. H. Cheng, *Adv. Energy Mater.*, 2024, **14**, 2400313.
- 18 S. Ding, H. Zhai, X. L. Tao, P. Yang, Z. Q. Liu, S. Y. Qin, Z. Y. Hong, X. Y. Chen and Z. L. Wang, *Small*, 2024, **20**, 2403879.
- 19 F. B. Xi, Y. K. Pang, G. X. Liu, S. W. Wang, W. Li, C. Zhang and Z. L. Wang, *Nano Energy*, 2019, **61**, 1–9.
- 20 C. Zhang, W. Yuan, B. Zhang, O. Yang, Y. Liu, L. He, J. Wang and Z. L. Wang, *Adv. Funct. Mater.*, 2022, **32**, 2111775.
- 21 W. Yuan, B. F. Zhang, C. G. Zhang, O. Yang, Y. B. Liu, L. X. He, L. L. Zhou, Z. H. Zhao, J. Wang and Z. L. Wang, *One Earth*, 2022, **5**, 1055–1063.
- 22 Z. Q. Xu, L. T. Chen, Z. Zhang, J. J. Han, P. F. Chen, Z. Y. Hong, T. Jiang and Z. L. Wang, *Small*, 2023, **19**, 2307288.
- 23 T. Jiang, H. Pang, J. An, P. J. Lu, Y. W. Feng, X. Liang, W. Zhong and Z. L. Wang, *Adv. Energy Mater.*, 2020, **10**, 2000064.
- 24 S. Panda, S. Hajra, Y. Oh, W. Oh, J. Lee, H. Shin, V. Vivekananthan, Y. Yang, Y. K. Mishra and H. J. Kim, *Small*, 2023, **19**, 2300847.
- 25 H. Hong, X. Yang, H. Cui, D. Zheng, H. Wen, R. Huang, L. Liu, J. Duan and Q. Tang, *Energy Environ. Sci.*, 2022, **15**, 621–632.
- 26 C. H. Song, X. Zhu, M. L. Wang, P. Yang, L. K. Chen, L. Hong and W. C. Cui, *Sustainable Energy Technol. Assess.*, 2022, **53**, 102767.
- 27 B. Y. Zhu, H. Wu, H. Q. Wang, Z. T. Quan, H. Luo, L. J. Yang, R. J. Liao and J. Y. Wang, *Nano Energy*, 2024, **124**, 109446.
- 28 Y. L. Zi, H. Y. Guo, Z. Wen, M. H. Yeh, C. G. Hu and Z. L. Wang, *ACS Nano*, 2016, **10**, 4797–4805.
- 29 L.-C. Zhao, H.-X. Zou, X. Xie, D.-H. Guo, Q.-H. Gao, Z.-Y. Wu, G. Yan, K.-X. Wei and W.-M. Zhang, *Nano Energy*, 2023, **108**, 108222.
- 30 Q. W. Wang, X. Yu, J. L. Wang, Y. Yu, Z. J. Wang, Z. L. Wang and T. H. Cheng, *Adv. Energy Mater.*, 2023, **13**, 2203707.
- 31 J. Feng, H. Zhou, Z. Cao, E. Zhang, S. Xu, W. Li, H. Yao, L. Wan and G. Liu, *Adv. Sci.*, 2022, **9**, 2204407.
- 32 H. Qiu, H. Wang, L. Xu, M. Zheng and Z. L. Wang, *Energy Environ. Sci.*, 2023, **16**, 473–483.
- 33 G. Li, J. Wang, S. K. Fu, C. C. Shan, H. Y. Wu, S. S. An, Y. Du, W. C. He, Z. Wang, W. L. Liu, Y. J. Nie, S. Y. Liu, P. Wang and C. G. Hu, *Adv. Funct. Mater.*, 2023, **33**, 2213893.
- 34 J. Y. Wang, Z. Y. Wu, L. Pan, R. J. Gao, B. B. Zhang, L. J. Yang, H. Y. Guo, R. J. Liao and Z. L. Wang, *ACS Nano*, 2019, **13**, 2587–2598.
- 35 J. L. Wang, H. Y. Li, D. Zhao, Q. Gao, X. J. Cheng, J. M. Wen, Z. L. Wang and T. H. Cheng, *Adv. Mater. Technol.*, 2023, **8**, 2300480.
- 36 X. Liang, S. Liu, Z. Ren, T. Jiang and Z. L. Wang, *Adv. Funct. Mater.*, 2022, **32**, 2205313.
- 37 M. Y. Xu, T. C. Zhao, C. Wang, S. L. Zhang, Z. Li, X. X. Pan and Z. L. Wang, *ACS Nano*, 2019, **13**, 1932–1939.
- 38 C. C. Han, Z. Cao, Z. H. Yuan, Z. W. Zhang, X. Q. Huo, L. A. Zhang, Z. Y. Wu and Z. L. Wang, *Adv. Funct. Mater.*, 2022, **32**, 2205011.
- 39 C. G. Zhang, L. L. Zhou, P. Cheng, D. Liu, C. L. Zhang, X. Y. Li, S. X. Li, J. Wang and Z. L. Wang, *Adv. Energy Mater.*, 2021, **11**, 2003616.
- 40 C. Zhang, Z. Zhao, O. Yang, W. Yuan, L. Zhou, X. Yin, L. Liu, Y. Li, Z. L. Wang and J. Wang, *Adv. Mater. Technol.*, 2020, **5**, 2000531.